## Unexpectedly large remanent polarization of Hf<sub>0.5</sub>Zr<sub>0.5</sub>O<sub>2</sub> metal-ferroelectric-metal capacitor fabricated without breaking vacuum

Cite as: Appl. Phys. Lett. 118, 012903 (2021); https://doi.org/10.1063/5.0029532 Submitted: 14 September 2020 . Accepted: 15 December 2020 . Published Online: 05 January 2021

🧓 Younghwan Lee, 🗓 H. Alex Hsain, Shelby S. Fields, Samantha T. Jaszewski, 🗓 Madison D. Horgan, Patrick G. Edgington, Don F. Ihlefeld, DGregory N. Parsons, and DJacob L. Jones











### Your Qubits. Measured.

Meet the next generation of quantum analyzers

- Readout for up to 64 qubits
- Operation at up to 8.5 GHz, mixer-calibration-free
- Signal optimization with minimal latency







# Unexpectedly large remanent polarization of Hf<sub>0.5</sub>Zr<sub>0.5</sub>O<sub>2</sub> metal-ferroelectric-metal capacitor fabricated without breaking vacuum

Cite as: Appl. Phys. Lett. **118**, 012903 (2021); doi: 10.1063/5.0029532 Submitted: 14 September 2020 · Accepted: 15 December 2020 · Published Online: 5 January 2021







Younghwan Lee,<sup>1,a)</sup> ID H. Alex Hsain,<sup>1</sup> ID Shelby S. Fields,<sup>2</sup> Samantha T. Jaszewski,<sup>2</sup> Madison D. Horgan,<sup>1</sup> ID Patrick G. Edgington,<sup>1</sup> Jon F. Ihlefeld,<sup>2,3</sup> ID Gregory N. Parsons,<sup>4</sup> ID and Jacob L. Jones<sup>1,a)</sup> ID

#### **AFFILIATIONS**

- Department of Materials Science and Engineering, North Carolina State University, Raleigh, North Carolina 27695, USA
- <sup>2</sup>Department of Materials Science and Engineering, University of Virginia, Charlottesville, Virginia 22904, USA
- <sup>3</sup>Department of Electrical and Computer Engineering, University of Virginia, Charlottesville, Virginia 22904, USA

Note: This paper is part of the Special Topic on Materials and Devices Utilizing Ferroelectricity in Halfnium Oxide.

<sup>a)</sup>Authors to whom correspondence should be addressed: ylee22@ncsu.edu and jacobjones@ncsu.edu

#### **ABSTRACT**

We introduce an Atomic Layer Deposition (ALD) technique referred to here as Sequential, No-Atmosphere Processing (SNAP) to fabricate ferroelectric  $H_{0.5}Zr_{0.5}O_2$  capacitors in Metal–Ferroelectric–Metal (MFM) structures. SNAP involves the ALD of each layer sequentially while maintaining the sample under vacuum process conditions without ambient exposure during the entire sequential deposition processes. We first use plasma enhanced ALD to fabricate 002-textured TiN films and study the degree of texture and quality of the film by X-ray Diffraction (XRD), Time-of-Flight Secondary Ion Mass Spectrometry (ToF-SIMS), and transmission electron microscopy. Building upon the textured TiN film, we fabricate MFM capacitors with 10-nm-thick  $H_{0.5}Zr_{0.5}O_2$  via SNAP deposition and observe an unexpectedly large remanent polarization ( $2P_r = 54.2 \ \mu C/cm^2$ ). We report that annealing at T <800 °C and at T = 800 °C results in different ferroelectric behaviors and phases determined by grazing incidence XRD patterns. We infer that the nonpolar tetragonal phase is dominant in films treated at T <800 °C, whereas the polar orthorhombic phase is dominant in films treated at T = 800 °C. Using ToF-SIMS and x-ray spectroscopy depth profiling on MFM capacitors, we observe an increase in the concentration of defects in the  $H_{0.5}Zr_{0.5}O_2$  layer after annealing. We believe that the absence of the native passive layer between  $H_{0.5}Zr_{0.5}O_2$  and TiN layers made via SNAP deposition is responsible for the unexpectedly large remanent polarization. In addition, we associate the 002-textured TiN as potentially playing a role in realizing the unexpectedly large remanent polarization.

Published under license by AIP Publishing. https://doi.org/10.1063/5.0029532

After the first discovery of ferroelectric HfO<sub>2</sub> in 2011, <sup>1</sup> it is generally accepted that a noncentrosymmetric space group of orthorhombic HfO<sub>2</sub> (*Pca*2<sub>1</sub>) describes the crystallographic structure, which has symmetry elements that allow for ferroelectricity. Although the polar phase of HfO<sub>2</sub> has been experimentally confirmed by other groups, <sup>2</sup> the main driving factors to obtain the polar phase are still in debate. It is believed that driving factors including dopants, <sup>1,3</sup> oxygen vacancies, <sup>4-6</sup> grain size, <sup>7</sup> thickness, <sup>7,8</sup> capping layer, <sup>1</sup> and annealing condition <sup>9</sup> influence the appearance of ferroelectricity.

The binary oxide system of HfO<sub>2</sub>–ZrO<sub>2</sub> has been intensely studied not only because of the structural similarities between HfO<sub>2</sub> and ZrO<sub>2</sub> but also because multiple functionalities such as dielectric,

ferroelectric, and antiferroelectric properties can be achieved by simply changing the chemical composition of  $(Hf_xZr_{1-x})O_2$  (HZO). Numerous studies suggest that a chemical composition around a 1:1 ratio (Hf:Zr) shows the most prominent ferroelectric properties. <sup>7,10</sup> Several deposition methods were studied to fabricate ferroelectric HZO thin films including Atomic Layer Deposition (ALD), <sup>11</sup> physical vapor deposition, <sup>12</sup> chemical vapor deposition, <sup>13</sup> pulsed laser deposition, <sup>14</sup> and chemical solution deposition. <sup>15</sup> ALD has been commonly used to deposit HZO thin films since the chemical composition of HZO can be easily controlled by the ratio of Hf and Zr precursor cycles, which enables homogenous chemical distribution uniformly in all directions and precise thickness control across the entire film.

Department of Chemical and Biomolecular Engineering, North Carolina State University, Raleigh, North Carolina 27695, USA

The desired polar phase can be induced by the Metal-Ferroelectric-Metal (MFM) structure. It is believed that mechanical confinement from the capping layer prevents volumetric expansion of HfO2 and enables shearing of the HfO2 unit cell, thereby generating ferroelectricity in HfO<sub>2</sub>-based materials. Various materials have been utilized as effective capping layers including Pt,16 RuO2,17 TaN,6 W,18 and Ir/IrO<sub>x</sub>. 19 It has been reported that approximately 74% of published papers (up to 2018)<sup>20</sup> used titanium nitride (TiN) as the capping layer for HZO capacitors because TiN generally shows better ferroelectricity than most other capping layers except for TaN. 12,16 However, the exact role of TiN in demonstrating better ferroelectric properties and the interface between TiN and HZO layers in HZO capacitors is still not well understood. In fact, few studies elaborate on the characteristics and experimental procedures to prepare their TiN in detail. Notably, a passive layer at a metal-ferroelectric interface can negatively influence ferroelectric properties. 21,22 Moreover, the preferred orientation of TiN films can be controlled via ALD deposition conditions,<sup>23</sup> which can influence the subsequent HZO characteristics. It is, therefore, reasonable to hypothesize that the bottom TiN electrode and the quality of the interface can influence ferroelectricity of HZO in various ways.

In the present study, we first demonstrate synthesis of 002-textured TiN via Plasma Enhanced Atomic Layer Deposition (PEALD)<sup>23</sup> and examine TiN properties. In addition, we introduce an unconventional deposition approach that we describe as Sequential, No-Atmosphere Processing (SNAP), where the bottom TiN, ferroelectric Hf<sub>0.5</sub>Zr<sub>0.5</sub>O<sub>2</sub> and top TiN are formed in sequence, without exposure to the ambient atmosphere. We emphasize the importance of the interface quality between TiN and Hf<sub>0.5</sub>Zr<sub>0.5</sub>O<sub>2</sub> and the uniqueness of using 002-textured TiN as top and bottom electrodes as well as a capping layer. We also report an unexpectedly large remanent polarization (2P<sub>r</sub> = 54.2  $\mu$ C/cm²) observed for SNAP-deposited MFM capacitors.

MFM capacitors were deposited on SiO<sub>2</sub>/Si substrates (VA semiconductors) after cleaning in an isopropyl ultrasonic bath for 5 min. Tetrakis(dimethylamido)hafnium(IV) (TDMAH), tetrakis(dimethylamido)zirconium(IV) (TDMAZ), and tetrakis(dimethylamido)titanium(IV) (TDMAT) were used as precursors, and H<sub>2</sub>O was chosen for an oxygen source. It should be noted that TDMAT, instead of TiCl<sub>4</sub>, which is another commonly used precursor to deposit TiN in PEALD, was chosen particularly to prevent halide contamination to the sample and corrosion to the ALD chamber.<sup>23</sup> Ar gas with a flow rate of 110 sccm was used to deliver all precursors and H2O to the ALD chamber, and a combination of Ar and N2 gas with flow rates of 10 and 20 sccm, respectively, was used to generate plasma during TiN deposition. The temperatures for all precursors, the delivery line, and the ALD chamber were maintained at 75, 150, and 270 °C, respectively, during the entire MFM capacitor fabrication process. TiN was deposited via PEALD in the ALD chamber (Fiji G2, Ultratech/ Cambridge) using TDMAT with pressures of ~0.1 Torr for precursor half-cycles and ~0.01 Torr for plasma half-cycles. For the plasma halfcycles, a plasma power of 250 W and a plasma pulse period of 20 s were used. Hf<sub>0.5</sub>Zr<sub>0.5</sub>O<sub>2</sub> was deposited as the ferroelectric layer via thermal ALD with a chamber pressure of ~0.4 Torr, alternating TDMAH and TDMAZ super cycles in a 1:1 ratio. The resulting MFM capacitors were then annealed via the Rapid Thermal Annealing (RTA) process with a ramp rate of 10 °C/s and a hold time of 30 s at various temperatures (AnnealSys AS-One).

The X-ray Diffraction (XRD) pattern of the TiN film was measured with Bragg-Brentano geometry, and the results are shown in Fig. 1(a). A cross-sectional Transmission Electron Microscopy (TEM) image of the TiN film used in the XRD measurement, shown in Fig. 1(b), indicates that the thickness of the film is approximately 35 nm. The absence of the 111 reflection of TiN ( $\sim$ 36.7°) and the appearance of 002 reflection of TiN (~42.6°) confirm that the TiN film is preferentially oriented with the (002) plane parallel to the surface. Figure 1(c) shows the Selected Area Electron Diffraction (SAED) patterns of TiN. Diffraction patterns marked with white circles correspond to the patterns of silicon along the [101] zone axis. The white arrow pointing to the arc-shaped diffraction pattern confirms a relatively strong degree of fiber texture in the (002) plane of the TiN film. To investigate chemical quality of 002-textured TiN, Time-of-Flight Secondary Ion Mass Spectrometry (ToF-SIMS) depth-profiling was performed and the results are shown in Fig. 1(d). Note that <sup>47</sup>TiN and 50TiO were used to discern mass interference between TiN and TiO. A relatively high <sup>50</sup>TiO<sup>-</sup> intensity at the top surface of the film indicates ambient oxidation of top TiN. The homogeneous and uniform chemical distribution of <sup>47</sup>TiN<sup>-</sup> confirms good chemical quality of TiN. Since most HZO capacitors with TiN capping layers undergo RTA processing at relatively high temperatures, XRD of the TiN film was measured as a function of temperature, in situ, during heating in the N<sub>2</sub> environment. Figure 1(e) shows XRD patterns of the TiN film measured as a function of temperature. The 002 reflection of TiN appears at temperatures up to 780 °C and then disappears at higher temperatures, which demonstrates that the 002 texture is stable up to 780 °C. The disappearance of the 002 reflection peak of TiN and

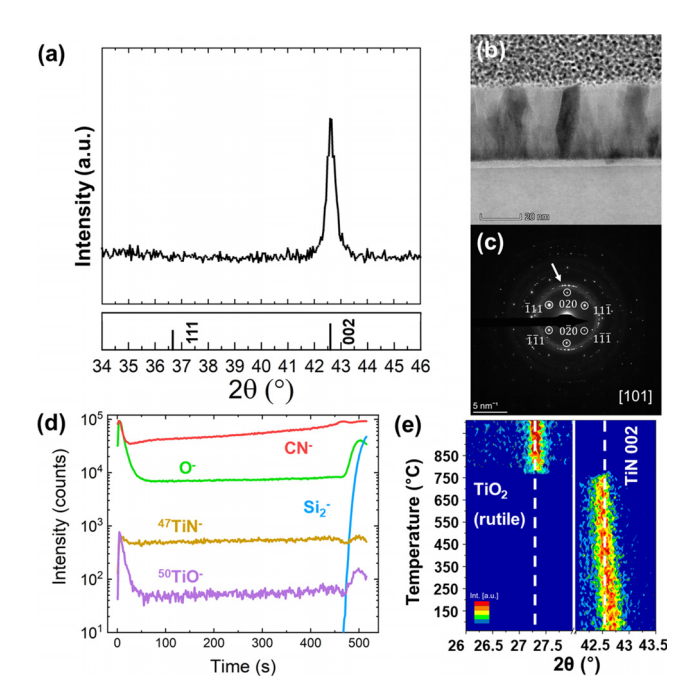


**FIG. 1.** Structural and chemical characterization results of 002-textured TiN. (a) XRD pattern (Bragg-Brentano geometry), (b) cross-sectional TEM image, (c) corresponding SAED, (d) ToF-SIMS depth-profile, and (e) XRD patterns measured as a function of temperature.

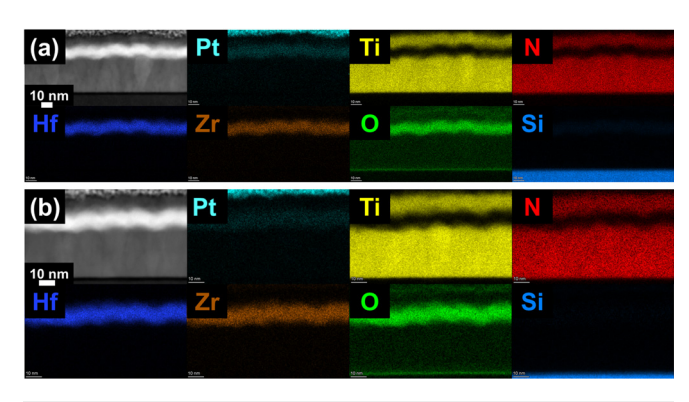


FIG. 2. Cross-sectional HAADF-STEM image and EDS elemental maps of (a) as-deposited and (b) 800  $^{\circ}$ C-annealed TiN(10 nm)/Hf<sub>0.5</sub>Zr<sub>0.5</sub>O<sub>2</sub>(10 nm)/TiN(30 nm).

emergence of a new peak ( $\sim$ 27.5°) at 780 °C suggest that TiN oxidizes to the rutile phase of TiO<sub>2</sub> at 780 °C. <sup>24,25</sup> Using a four-point probe, the DC resistivity of the 002-textured TiN film was measured to be 185.5  $\mu\Omega$ ·cm, which is sufficiently low for good electrode performance. <sup>26</sup> The low resistivity of TiN coupled with high thermal stability and chemical quality suggested by *in situ* XRD and ToF-SIMS, respectively, indicates that PEALD-fabricated TiN may serve as an adequate electrode and a capping layer for HZO capacitors.

Figure 2 shows High Angle Annular Dark Field (HAADF) images from the Scanning Transmission Electron Microscopy (STEM) and Electron Dispersive Spectroscopy (EDS) elemental maps of the asdeposited and 800 °C-annealed MFM capacitors. Note that an annealing temperature of 800 °C is chosen because this temperature is expected to induce a phase transformation from the nonpolar tetragonal to polar orthorhombic phase based on our previous study. <sup>25</sup> As expected, Ti and N appear mostly in top and bottom layers, while Hf, Zr, and O appear in the intermediate layer. These results indicate that the SNAP deposition yields an excellent quality of MFM capacitors that exhibit desirable homogeneous chemical distributions and sharp interfaces between the TiN and Hf<sub>0.5</sub>Zr<sub>0.5</sub>O<sub>2</sub> layers at both the top and bottom interfaces, even after RTA processing.

Figure 3(a) shows Polarization vs Electric Field (P–E) loops obtained from MFM capacitors with several annealing temperatures. As the annealing temperature increases, the P–E loops start to open and show typical hysteresis loop behavior. The 2P<sub>r</sub> values measured via Positive Up Negative Down (PUND) measurements were 25.8, 34.6, and  $54.2\,\mu\text{C/cm}^2$  for the capacitors annealed at 400, 600, and  $800\,^{\circ}\text{C}$ , respectively. Figure 3(b) shows that the switching current double peaks, present in the vicinity of the coercive fields in the capacitors annealed at 400 and 600 °C, are observed to merge into a single and intense peak at the coercive fields in the capacitor annealed at 800 °C. Figure 3(c) shows small signal Capacitance–Voltage (C–V) results, which indicate that relative permittivity varies in capacitors annealed

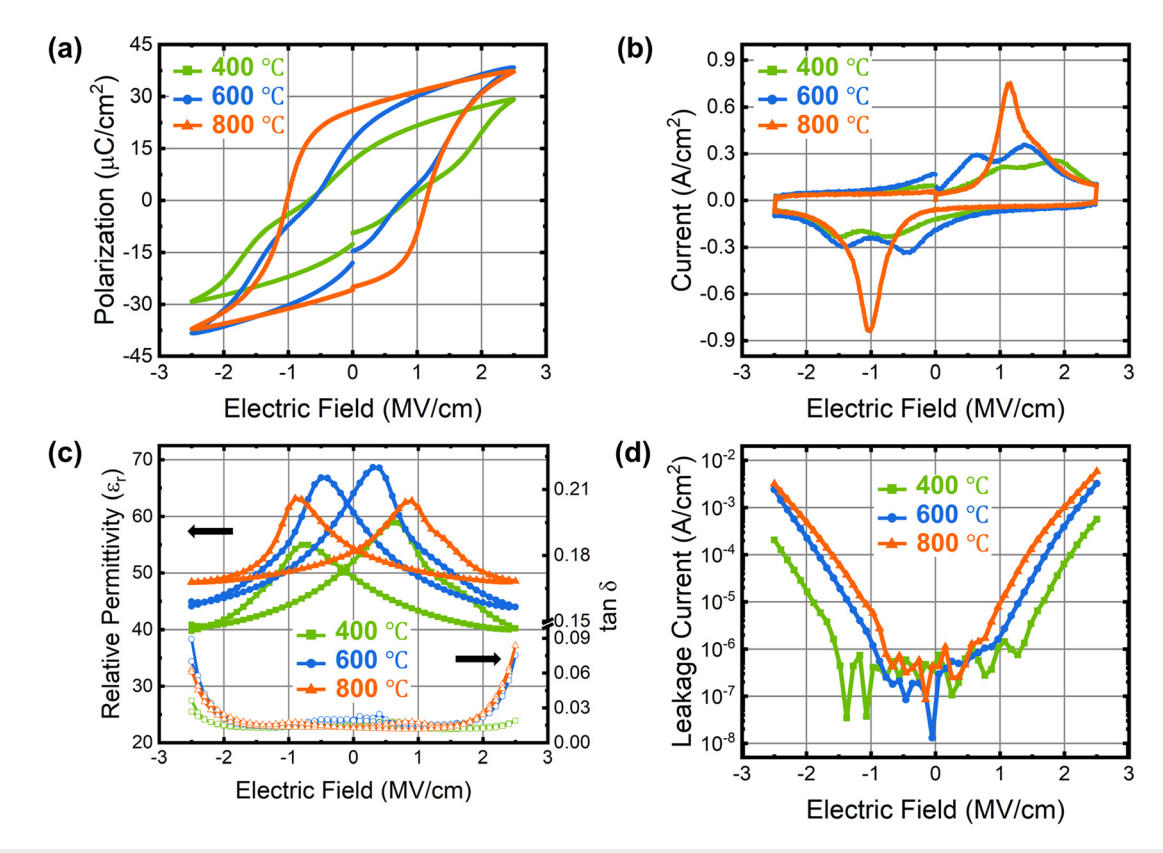


FIG. 3. (a) P-E hysteresis loop, (b) switching current loop, (c) small signal C-V measurement, and (d) leakage current results of MFM capacitors annealed at different temperatures.

at different temperatures. In particular, the capacitor annealed at 600 °C shows the largest relative permittivity at zero DC bias (i.e., the intercept with the vertical axis). Given that the relative permittivity of the tetragonal phase is typically higher than that of monoclinic and orthorhombic phases,<sup>27</sup> it is expected that the tetragonal phase would be more dominant relative to the other phases in the capacitor annealed at 600 °C. Figure 3(d) shows that the leakage currents increase as the annealing temperature increases from 400 to 800 °C. The increase in the leakage current is typically understood as the increase in the concentration of defects in MFM capacitors. 4,5 Note that the concentration of defects, such as nitrogen<sup>3</sup> or vacancies of oxygen, 4-6 can significantly influence the stabilization of the polar orthorhombic phase of Hf<sub>0.5</sub>Zr<sub>0.5</sub>O<sub>2</sub>, thereby promoting resultant ferroelectricity. Hence, it is reasonable to hypothesize that the increase in 2P<sub>r</sub> at higher annealing temperature is caused by the stabilization of the orthorhombic phase, which originates from the increase in the concentration of defects. To test this hypothesis, we performed several additional structural and chemical characterization experiments on MFM capacitors annealed at various temperatures.

Figure 4 shows GIXRD patterns of MFM capacitors annealed at different temperatures. Magnified images of the  $Hf_{0.5}Zr_{0.5}O_2$  peaks are shown on the right (27.0° to 34.0°). Detailed analysis of peak fittings at different annealing temperatures are shown in Fig. S1. Note that the  $2\theta$  positions of the highest intensity peak of the orthorhombic and tetragonal phases of  $Hf_{0.5}Zr_{0.5}O_2$ , expected at 29.9° and 30.3°, are

difficult to discriminate due to the peak overlap, respectively. However, knowing that the orthorhombic peak lies at a lower  $2\theta$  value than the tetragonal peak, a peak shift toward lower  $2\theta$  is often interpreted as an increase in the orthorhombic phase fraction.<sup>24,25</sup> The broad peak profile of the as-deposited capacitor indicates that the starting Hf<sub>0.5</sub>Zr<sub>0.5</sub>O<sub>2</sub> is amorphous according to XRD. No peaks are observed near  $\sim 28.3^{\circ}$  and  $\sim 31.7^{\circ}$ , indicating that the monoclinic phase is well suppressed throughout all annealing temperatures up to 800 °C. After annealing at 400 °C, a strong XRD peak emerges at 30.8°, indicating that Hf<sub>0.5</sub>Zr<sub>0.5</sub>O<sub>2</sub> crystallizes primarily in the tetragonal phase. In particular, a peak shift toward lower  $2\theta$  ( $\sim$ 0.2°) is observed from 600 to 800 °C. Therefore, it is expected that the orthorhombic phase fraction would be largest at 800 °C. 24,25 These results are consistent with the electrical characterization results, which show larger 2P<sub>r</sub> and smaller relative permittivity in the capacitors annealed at 800 °C vs the one annealed at 600 °C.

To study the interface between TiN and  $Hf_{0.5}Zr_{0.5}O_2$  and the chemical change in the  $Hf_{0.5}Zr_{0.5}O_2$  layer at different annealing temperatures more precisely, samples of larger thickness were fabricated using SNAP where the thicknesses of the top and bottom TiN and  $Hf_{0.5}Zr_{0.5}O_2$  are all 30 nm. Figures 5(a)-5(c) show ToF-SIMS depth profiles of thicker MFM samples annealed at different temperatures. The consistent intensity profile of  $^{47}\text{TiN}^-$  for all samples indicates that the top and bottom TiN layers are chemically stable after RTA processing. The increase in  $^{50}\text{TiO}^-$  intensity from 0 to 100 s in Fig. 5(c)

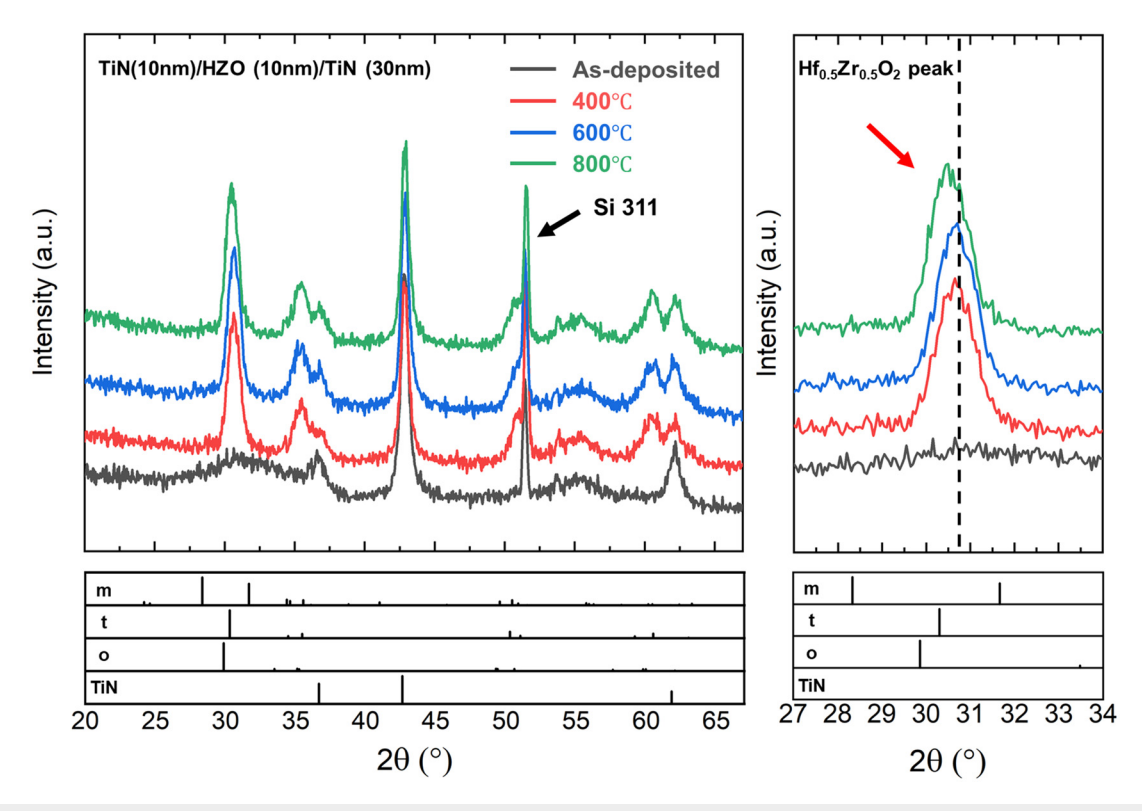


**FIG. 4.** GIXRD patterns of TiN(10 nm)/Hf<sub>0.5</sub>Zr<sub>0.5</sub>O<sub>2</sub>(10 nm)/TiN(30 nm) after various annealing treatments (left) and in the magnified  $2\theta$  range of  $27^{\circ}$  to  $34^{\circ}$  (right). The reference XRD patterns of Hf<sub>0.5</sub>Zr<sub>0.5</sub>O<sub>2</sub> phases used in this study are as follows: orthorhombic (PDF #: 04-005-5597), tetragonal (PDF #: 04-011-8820), and monoclinic (PDF #: 00-034-0104). Note that peaks with relative intensity less than 5% from the reference pattern were omitted.

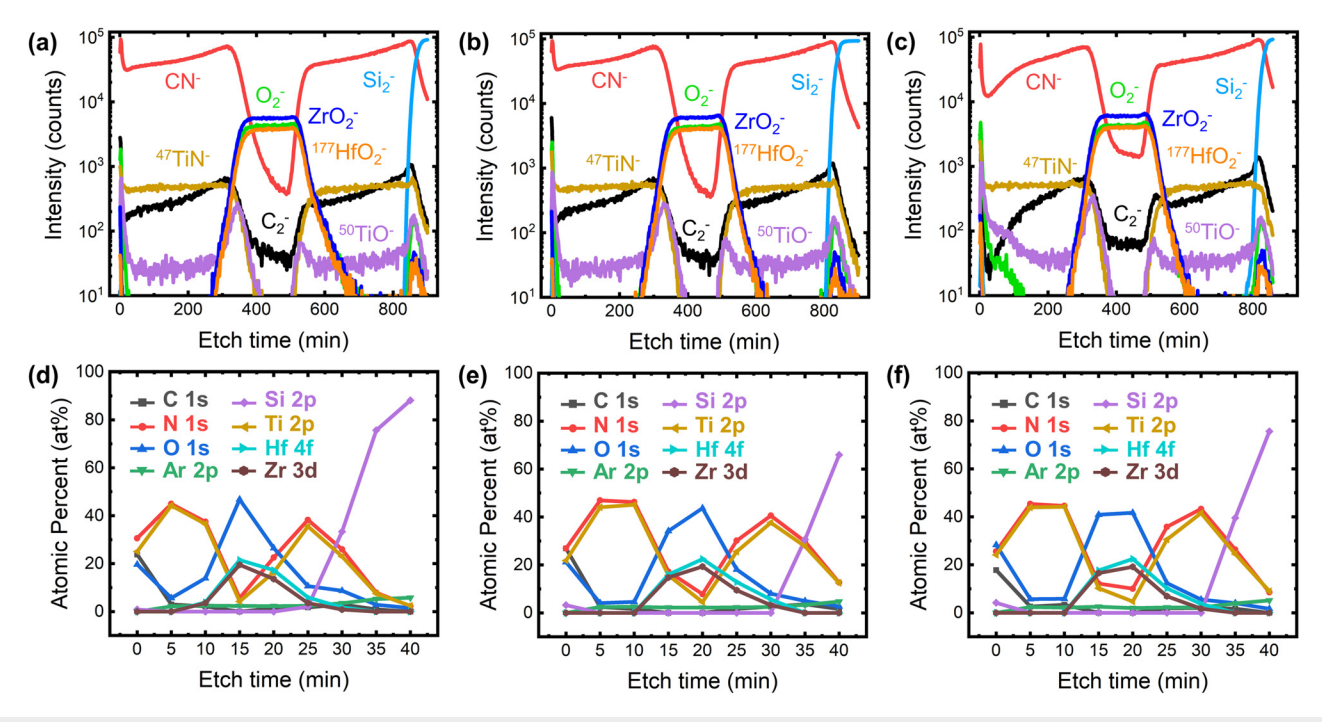


FIG. 5. (a)–(c) ToF-SIMS and (d)–(f) XPS depth profiles of TiN(30 nm)/Hf<sub>0.5</sub>Zr<sub>0.5</sub>O<sub>2</sub>(30 nm)/TiN(30 nm) at different annealing temperatures: as-deposited (a) and (d),  $500 \,^{\circ}$ C (b) and (e), and  $800 \,^{\circ}$ C (c) and (f). The 68.3% confidence intervals for all elements in the XPS analysis are less than 0.5 at. %.

implies that  ${\rm TiO_2}$  oxidation had occurred at  $800\,^{\circ}{\rm C}$  preferentially from the top surface. It should be noted that both  ${\rm C_2}^-$  and  ${\rm CN}^-$  intensities increased in the  ${\rm Hf_{0.5}Zr_{0.5}O_2}$  layer at  $800\,^{\circ}{\rm C}$ , which indicates carbon and nitrogen diffusion during RTA processing. X-ray Photoelectron Spectroscopy (XPS) depth profiles were also acquired for the MFM samples annealed at different temperatures and are plotted in Figs. 5(d)–5(f). Detailed elemental quantification of the  ${\rm Hf_{0.5}Zr_{0.5}O_2}$  layer is summarized in Table I. Interestingly, the O 1s concentration gradually decreases and the N 1s concentration gradually increases as annealing temperature increases. The decrease in the O 1s concentration and increase in nonstoichiometric TiN (indicated by an increase in the N 1s concentration) may indicate an increase in oxygen vacancies in, and nitrogen diffusion into, the  ${\rm Hf_{0.5}Zr_{0.5}O_2}$  layer at higher annealing temperatures. This observation is consistent with the increase in  ${\rm CN}^-$  intensity at the  ${\rm Hf_{0.5}Zr_{0.5}O_2}$  layer for the

**TABLE I.** XPS quantification of elements in the  $Hf_{0.5}Zr_{0.5}O_2$  layer before annealing and after two different annealing temperatures. Note that the atomic percent is displayed with 68.3% confidence intervals.

	As-deposited (at. %)	500 °C (at. %)	800 °C (at. %)
Hf 4f	$21.53 \pm 0.16$	$22.46 \pm 0.18$	$22.45 \pm 0.16$
Zr 3d	$19.52 \pm 0.26$	$19.32 \pm 0.17$	$19.17 \pm 0.15$
O 1s	$46.80 \pm 0.34$	$43.66 \pm 0.35$	$41.66 \pm 0.31$
N 1s	$5.62 \pm 0.36$	$7.80 \pm 0.41$	$10.06 \pm 0.34$
Ti 2p	$4.20 \pm 0.16$	$4.53 \pm 0.16$	$4.72 \pm 0.16$
Ar 2p	$2.33 \pm 0.24$	$2.23 \pm 0.26$	$1.95 \pm 0.21$

 $800\,^{\circ}\text{C}$ -annealed MFM sample from the ToF-SIMS depth-profile result. The increase in leakage current for the  $800\,^{\circ}\text{C}$ -annealed capacitor shown in Fig. 3(d) corroborates the observed increase in the concentration of defects. Therefore, the combination of chemical and electrical analyses suggests that the incorporation of defects including carbon, nitrogen, and vacancies of oxygen upon annealing at  $800\,^{\circ}\text{C}$  may help to stabilize the orthorhombic phase relative to the tetragonal phase in the  $Hf_{0.5}Zr_{0.5}O_2$  layer, resulting in a larger  $2P_r$  extracted from the PUND measurement.

Considering that the largest value for the remanent polarization previously reported for HZO (nominally without the dopant) is  $2P_r=50.9~\mu C/cm^2,^{20}$  our remanent polarization  $(2P_r=54.2~\mu C/cm^2)$  represents a notable (nearly 10%) increase. This large value for remanent polarization may be ascribed to one or both the following factors: (1) the clean interfaces between TiN and the  $Hf_{0.5}Zr_{0.5}O_2$  layer created via the SNAP method and (2) the 002 texture in the top and bottom TiN electrodes.

As shown in the EDS results, the sharp interface between the TiN and  $Hf_{0.5}Zr_{0.5}O_2$  layers is a direct result of the SNAP deposition, which prevents exposure to the ambient atmosphere during sequential deposition of the MFM stack. Most studies of ferroelectric  $HfO_2$ -based thin films use ALD for  $HfO_2$  deposition and reactive sputtering for the TiN deposition. Thus, the bottom TiN film is exposed to the ambient atmosphere during transfer to the ALD chamber. This exposure to the ambient atmosphere enables the growth of a native oxide ( $TiO_x$  or  $TiO_xN_y$ )<sup>4,27</sup> on the bottom TiN layer. This additional oxide layer can be considered as a passive layer in the MFM capacitor, which can substantially influence the switching characteristics. For example, for a ferroelectric capacitor that has values of  $P_r = 20 \ \mu C/cm^2$  and

 $E_c=100\,kV/cm$ , a thin passive layer with  $d/(L\cdot\epsilon_d)\approx 10^{-3}$  can suppress  $P_r$  by a factor of 2, where L and d are thicknesses of ferroelectric and passive layers and  $\epsilon_d$  is the relative permittivity of the passive layer. Therefore, the clean interface between the TiN and  $Hf_{O.5}Zr_{0.5}O_2$  layer, achieved by maintaining the sample under vacuum conditions throughout the SNAP process, mitigates the growth of detrimental passive layers, thereby promoting large remanent polarization. The P–E and  $2P_r$  results of non-SNAP-deposited capacitors, i.e., a control experiment in which vacuum is purposefully broken after every layer is deposited, are shown in Fig. S2. The poorer ferroelectric properties of the non-SNAP sample reinforce the important effect of sequential deposition under the vacuum condition. These results indicate that SNAP deposition plays an important role in maximizing the remanent polarization.

Another possible factor contributing to the large remanent polarization lies in the effect of 002-textured TiN. We note that TiN has a rock salt crystal structure where both Ti and N occupy a face-centered cubic sublattice. It is worth considering the possible atomic terminations of the (00h)-terminated surface, where h is an integer, compared to the other surfaces of TiN. The (00h)-terminated surface of TiN consists of both Ti and N atoms showing uniform Ti-N bonding on top of the surface, whereas a (111)-terminated surface of TiN consists of either Ti or N atoms, enabling either only Ti-Ti or N-N bonding. Thus, it is expected that the homogenous and periodic arrangement of Ti and N atoms on an (00h)-terminated surface would provide a uniform source for nitrogen to diffuse from TiN into the Hf<sub>0.5</sub>Zr<sub>0.5</sub>O<sub>2</sub> layer during the annealing process. Given that both nitrogen incorporation and vacancies of oxygen are key driving factors that help to stabilize the orthorhombic phase and generate ferroelectricity in HfO2,3the large remanent polarization in our Hf<sub>0.5</sub>Zr<sub>0.5</sub>O<sub>2</sub>, MFM capacitor would be caused by the increase in the defect concentration during the annealing process, particularly at 800 °C.

In this study,  $Hf_{0.5}Zr_{0.5}O_2$  MFM capacitors were fabricated via SNAP deposition. An annealing temperature of 800 °C showed the largest orthorhombic phase fraction and a large remanent polarization of  $2P_r = 54.2 \ \mu\text{C/cm}^2$ . These results are explained by (1) the absence of the passive layer created in the SNAP deposition and (2) an increase in the concentration of defects such as carbon, nitrogen, and vacancies of oxygen within the  $Hf_{0.5}Zr_{0.5}O_2$  layer during RTA processing, partly supported by the use of 002-textured TiN.

See the supplementary material for details of electrode pattern fabrication and structural and electrical characterization conditions.

This contribution is based upon the work supported by the National Science Foundation, as part of the Center for Dielectrics and Piezoelectrics under Grant Nos. IIP-1841453 and IIP-1841466. H.A.H. was supported by the National Science Foundation Graduate Research Fellowship Program (No. DGE-1746939). S.T.J. was supported by the National Science Foundation Graduate Research Fellowship Program (No. DGE-1842490). S.S.F., S.T.J., and J.F.I. acknowledge support from the Semiconductor Research Corporation's Global Research Collaboration program under task No. 2875.001. This work was performed at the Analytical Instrumentation Facility (AIF) at North Carolina State University, Shared Materials Instrumentation Facility (SMIF) at Duke University, and NC State Nanofabrication Facility (NNF), which

are supported by the State of North Carolina and the National Science Foundation (Award No. ECCS-2025064). AIF, SMIF and NNF are members of the North Carolina Research Triangle Nanotechnology Network (RTNN), a site in the National Nanotechnology Coordinated Infrastructure (NNCI).

#### **DATA AVAILABILITY**

The data that support the findings of this study are available within this article and its supplementary material.

#### **REFERENCES**

- <sup>1</sup>T. S. Böscke, J. Müller, D. Bräuhaus, U. Schröder, and U. Böttger, Appl. Phys. Lett. **99**, 112904 (2011).
- <sup>2</sup>X. Sang, E. D. Grimley, T. Schenk, U. Schroeder, and J. M. LeBeau, Appl. Phys. Lett. 106, 162905 (2015).
- <sup>3</sup>L. Xu, T. Nishimura, S. Shibayama, T. Yajima, S. Migita, and A. Toriumi, Appl. Phys. Express 9, 081201 (2016).
- <sup>4</sup>M. Pešić, F. P. G. Fengler, L. Larcher, A. Padovani, T. Schenk, E. D. Grimley, X. Sang, J. M. LeBeau, S. Slesazeck, U. Schroeder, and T. Mikolajick, Adv. Funct. Mater. 26, 4601 (2016).
- <sup>5</sup>A. Pal, V. K. Narasimhan, S. Weeks, K. Littau, D. Pramanik, and T. Chiang, Appl. Phys. Lett. **110**, 022903 (2017).
- <sup>6</sup>M. Hoffmann, U. Schroeder, T. Schenk, T. Shimizu, H. Funakubo, O. Sakata, D. Pohl, M. Drescher, C. Adelmann, R. Materlik, A. Kersch, and T. Mikolajick, J. Appl. Phys. 118, 072006 (2015).
- <sup>7</sup>M. H. Park, Y. H. Lee, H. J. Kim, T. Schenk, W. Lee, K. Do Kim, F. P. G. Fengler, T. Mikolajick, U. Schroeder, and C. S. Hwang, Nanoscale **9**, 9973 (2017).
- <sup>8</sup>P. Polakowski and J. Müller, Appl. Phys. Lett. **106**, 232905 (2015).
- <sup>9</sup>M. H. Park, Y. H. Lee, H. J. Kim, Y. J. Kim, T. Moon, K. Do Kim, J. Müller, A. Kersch, U. Schroeder, T. Mikolajick, and C. S. Hwang, Adv. Mater. 27, 1811 (2015).
- <sup>10</sup>J. Müller, T. S. Böscke, U. Schröder, S. Mueller, D. Bräuhaus, U. Böttger, L. Frey, and T. Mikolajick, Nano Lett. 12, 4318 (2012).
- <sup>11</sup>M. Materano, C. Richter, T. Mikolajick, and U. Schroeder, J. Vac. Sci. Technol., A 38, 022402 (2020).
- <sup>12</sup>T. Mittmann, M. Materano, P. D. Lomenzo, M. H. Park, I. Stolichnov, M. Cavalieri, C. Zhou, C. C. Chung, J. L. Jones, T. Szyjka, M. Müller, A. Kersch, T. Mikolajick, and U. Schroeder, Adv. Mater. Interfaces 6, 1901528 (2019).
- <sup>13</sup>T. Shimizu, T. Yokouchi, T. Shiraishi, T. Oikawa, P. S. S. Rama Krishnan, and H. Funakubo, Jpn. J. Appl. Phys., Part 1 53, 09PA04 (2014).
- 14T. Shimizu, T. Yokouchi, T. Oikawa, T. Shiraishi, T. Kiguchi, A. Akama, T. J. Konno, A. Gruverman, and H. Funakubo, Appl. Phys. Lett. 106, 112904 (2015).
  15S. Starschich, D. Griesche, T. Schneller, R. Waser, and H. Böttger, Appl. Phys.
- <sup>15</sup>S. Starschich, D. Griesche, T. Schneller, R. Waser, and U. Böttger, Appl. Phys. Lett. 104, 202903 (2014).
- <sup>16</sup>M. Hyuk Park, H. Joon Kim, Y. Jin Kim, W. Lee, T. Moon, and C. S. Hwang, Appl. Phys. Lett. **102**, 242905 (2013).
- <sup>17</sup>M. H. Park, H. J. Kim, Y. J. Kim, W. Jeon, T. Moon, and C. S. Hwang, Phys. Status Solidi-Rapid Res. Lett. 8, 532 (2014).
- <sup>18</sup>G. Karbasian, R. Dos Reis, A. K. Yadav, A. J. Tan, C. Hu, and S. Salahuddin, Appl. Phys. Lett. **111**, 022907 (2017).
- <sup>19</sup>P. D. Lomenzo, P. Zhao, Q. Takmeel, S. Moghaddam, T. Nishida, M. Nelson, C. M. Fancher, E. D. Grimley, X. Sang, J. M. LeBeau, and J. L. Jones, J. Vac. Sci. Technol., B 32, 03D123 (2014).
- <sup>20</sup>S. J. Kim, J. Mohan, S. R. Summerfelt, and J. Kim, J. Mater. 71, 246 (2019).
- <sup>21</sup>D. Damjanovic, Rep. Prog. Phys. **61**, 1267 (1998).
- <sup>22</sup>A. K. Tagantsev, M. Landivar, E. Colla, and N. Setter, J. Appl. Phys. 78, 2623 (1995).
- <sup>23</sup>I. Krylov, X. Xu, E. Zoubenko, K. Weinfeld, S. Boyeras, F. Palumbo, M. Eizenberg, and D. Ritter, J. Vac. Sci. Technol., A 36, 06A105 (2018).
- <sup>24</sup>M. H. Park, C. C. Chung, T. Schenk, C. Richter, K. Opsomer, C. Detavernier, C. Adelmann, J. L. Jones, T. Mikolajick, and U. Schroeder, Adv. Electron. Mater. 4, 1800091 (2018).
- <sup>25</sup>H. A. Hsain, Y. Lee, G. Parsons, and J. L. Jones, Appl. Phys. Lett. **116**, 192901 (2020).
- <sup>26</sup>M. G. Kozodaev, Y. Y. Lebedinskii, A. G. Chernikova, S. N. Polyakov, and A. M. Markeev, Phys. Status Solidi A 214, 1700056 (2017).
- <sup>27</sup>E. D. Grimley, T. Schenk, X. Sang, M. Pešić, U. Schroeder, T. Mikolajick, and J. M. LeBeau, Adv. Electron. Mater. 2, 1600173 (2016).